Available online at www.sciencedirect.com

ScienceDirect

Procedia Engineering 103 (2015) 205 – 212

Procedia Engineering

www.elsevier.com/locate/procedia

The 13th Hypervelocity Impact Symposium

Dynamic Brittle Fragmentation: Probing the Byproducts of Hypervelocity Impact in Space

James D. Hogan[a]*, Charles El Mir[b], Jeffrey B. Plescia[c], KT Ramesh[a.b]

a. Hopkins Extreme Materials Institute, the Johns Hopkins University, Baltimore MD 21218
b. Department of Mechanical Engineering, the Johns Hopkins University, Baltimore MD 21218
c. Applied Physics Laboratory, the Johns Hopkins University, Laurel, MD 20723

Abstract

Improvements in computational and analytical modelling of large-scale impact and catastrophic disruption events will come from a better understanding of the failure processes that are active during high strain-rate events. In this study we investigate the dynamic compressive failure and fragmentation of basalt, paying particular attention to the role each constituent mineral phase has in these processes. Our results indicate the existence of two fragmentation mechanisms: **I.** a mechanism that creates small fragments that is associated with the spacing of critically activated defects. These fragments are primarily comprised of pyroxene (which has the lowest fracture toughness in this material). **II.** a mechanism related to larger fragments that is associated with the structural failure of the sample. These fragments are primarily polyphase and polygrain in composition.

In the second part of the paper, we investigate the strength of fragmented basalt material for different initial fragment size distributions: 1. between 10 and 100 microns, 2. between 200 and 800 microns, and 3. between 300 and 1,800 microns. The porosity of each of the three samples was maintained between 30 and 35 %. Understanding the composition of the fragments beforehand allows us to better interpret our experimental results, which indicate that the strengths of the fragmented material increased with decreasing fragment sizes, from 4 to 25 MPa, and then to 175 MPa. An increase in strength with smaller fragment sizes is expected because of the associated increase in frictional dissipation, and decrease in the relative contribution of compaction and fracturing mechanisms. However, we do note that fragments less than 100 microns fail as a result of the activation of a different critical defect type than in the bulk material and for fragments larger than 100 microns, where olivine grains are the key contributors to fracture. Altogether, these results highlight the influence of the composition and defect population of planetary materials on the associated length scales that arise from dynamic failure and fragmentation.

Peer-review under responsibility of the Curators of the University of Missouri On behalf of the Missouri University of Science and Technology

Keywords: brittle fracture, planetary materials, dynamic fragmentation, granular behavior, basalt

Nomenclature

A	projected area of imaged fragment (m^2)
C	scaling parameter for power-law fit
D	fractal dimension for power-law fit
E	Young's modulus (Pa)
L	major axis dimension taken as the longest spanning dimension of a fragment in an image (m)
m	mass (kg)
n	scaling parameter for distribution fit
P	projected perimeter of imaged fragment (m)

* James Hogan. Tel.: 1-410-516-7257
E-mail address: jd.hogan@jhu.edu.

Peer-review under responsibility of the Curators of the University of Missouri On behalf of the Missouri University of Science and Technology
doi:10.1016/j.proeng.2015.04.028

s	half of the major axis dimension of a defect (m)
s'	scaling parameter for distribution fit (m)
	Greek symbols
ε	strain
σ	stress (Pa)
η	Defect density (#/m^2)
ρ	density (kg/m^3)
Φ	porosity
λ	ratio of outer and inner diameter of confinement tube
Subscripts	
c	confinement
gage	measurements associated with the gage section of the granular test container
intact	properties related to the solid basalt material
frag	properties related to the granular basalt material
min	minimum size
xx	axial strain
y	yield
yy	lateral strain

1. Introduction

Understanding the dynamic behavior of planetary materials is central in interpreting planetary impacts [1] and asteroid collisions [2]. The initial fragmentation byproducts of these hypervelocity events are dependent on the material microstructure (e.g., constituent phases and number of flaws) [3] and the complex multi-axial stress-loading history that manifests during impact. Additional fragmentation may occur from, for example, subsequent high-energy impact events (e.g., meteoroid bombardment) and through other mechanisms, such as thermal fatigue [4]. An improved understanding of the fragmentation of planetary materials, as well as the behavior and the evolution of these fragmented materials, will lead to more insight into the processes that govern large-scale impacts.

In this study, we investigate the dynamic fragmentation of intact and granular basalt. We choose basalt because it is the most common type of rock in the inner solar system [5], as well as in the main asteroid belt. We seek to understand the effect of the microstructure (e.g., constituent phases, defects) on the dynamic compressive failure and fragmentation of the intact material. Once key defects are identified, they are quantified using image analysis techniques and are then linked to fragment size distributions. Lastly, we investigate the strength of the granular basalt for different initial fragment size distributions, and discuss the implications in terms of the important length and time scales arising from failure and fragmentation of planetary materials.

2. Methods and Materials

Experiments on intact and granular basalt are performed at strain rates between 200 and 500 s^{-1} using a Kolsky bar apparatus. Impact simulations by Ernst et al. [6] showed that these are common strain rates in the vicinity of the impact site for a 5 km/s impact by a 1 km-sized object. Time-resolved failure of the intact sample is imaged using a Kirana high-speed camera filming at 2 million frames per seconds with a 100 ns exposure time. Digital image correlation techniques developed by Eberl et al. [7] are applied to the video images to measure the components of strain in the image. The Kolsky bar was used by Kimberley and Ramesh [8] in their study of the compressive strength of an ordinary chondrite and the setup is discussed therein. Cuboidal samples are used for the intact material geometry, approximately 3.5 mm x 4 mm x 5 mm in dimension. Fragments were collected after the experiments for examination, and subsequent dynamic experiments were performed on granular material samples consisting of three selected fragment size populations: 1. between 10 and 100 μm (mean of 26 ± 11 μm), 2. between 200 and 800 μm (mean of 408 ± 145 μm), and 3. between 300 and 1,800 μm (mean of 988 ± 422 μm). The granular fragments are encapsulated in heat shrink tubing with an outer diameter of 7.6 mm and an inner diameter of 7.4 mm. As the granular material undergoes deformation, the tubing applies a confinement pressure ($\sigma_{confinement}$: Pa) given by:

$$\sigma_{confinement} = \frac{\sigma_y}{2}[\lambda^2 - 1] \tag{1}$$

where σ_y is the yield strength of the confinement material (Pa), and λ is the ratio of the outer and inner diameter of the confinement tube. Here, σ_y= 10.3 MPa, and λ= 1.03, and, thus, $\sigma_{confinement}$= 314 kPa. Two hardened steel cylindrical plugs are inserted to contain the material. The material for the plugs matches that of the Kolsky bar, and the dimensions of the plugs are approximately 7 mm in diameter and 7 mm in length. The gage section of material being tested has diameter of 7 mm and its length is varied to maintain similar porosities depending on the initial average fragment size. Two copper pulse shapers that were 0.7 mm thick were used with a projectile length of 25.4 mm. Sample sizes and pulse shaping strategies were motivated by the work of Song et al. [9].

The basalt was purchased from Coverall Stone, WA. A polarized thin section image is shown in Figure 1a and an optical microscope image is shown in Figure 1b. Olivine (<500 μm and angular), pyroxene (<150 μm and darker in shade), and feldspar (<100 μm, light and needle-like structures) are highlighted in the images. Our basalt has a Young's modulus of 70 GPa and a density of 2,870 kg/m^3. Past Kolsky bar experiments involving this basalt have shown that it has a uniaxial compressive strength of 385 MPa at a strain rate of 10^{-3} s^{-1} and ~570 MPa at 950 s^{-1} [10]. It has a tensile strength, as measured using the Brazilian disk technique, of 60 MPa at 60 s^{-1} and 175 MPa at 22 s^{-1} [10].

A Zeiss optical microscope with an AxioCam MRC camera was used to image fragments after the experiments. Shown in Figure 1c are examples of basalt fragments derived during Kolsky bar testing at a strain rate of 430 s^{-1}. Images of fragments are converted to monochrome by threshholding (Figure 1d) and image processing techniques developed by Hogan et al. [11] are used to determine the major axis size (i.e., L: longest spanning), projected area (A), and perimeter (P). The bright-field images in Figure 1c are taken using the differential interference contrast settings to have the fragments appear dark. Additional dark-field images were taken to have the fragments appear in color. Pixels of fragments in the monochrome images are related to those in the colored images, and this allows us to determine the mean greyscale color intensity of individual fragments. We use this as an indicator of fragment composition. Similar image analysis techniques are also used to determine the spacing between the olivine grains, which are linked with fragment size distributions.

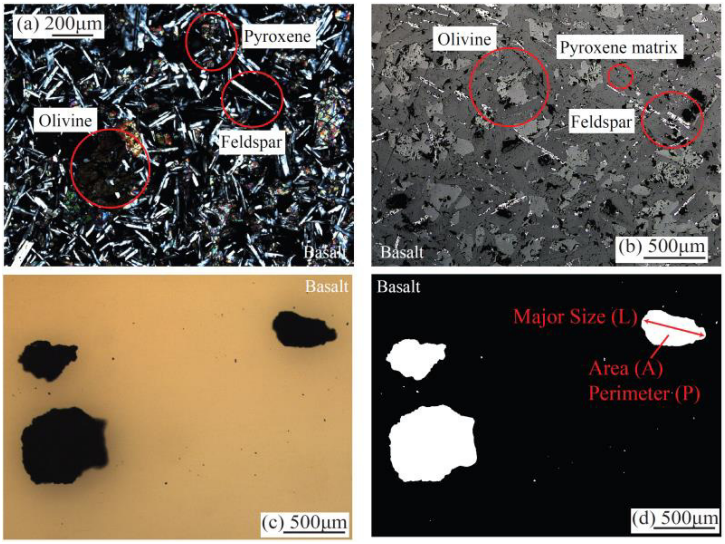

Fig. 1. (a) Polarized image of basalt thin section and (b) non-polarized surface image of basalt microstructure, both with constituent phases labelled. (c) Optical microscope image of basalt fragments and (d) converted monochrome image of basalt fragments with major axis size (L: m), area (A: m^2), and perimeter (P: m) labelled.

3. Experimental Results

3.1. Dynamic Failure of Intact Basalt

Initially, we examine the dynamic compressive failure of the intact basalt sample (Fig. 2). Shown on the left of Fig. 2 is the stress-time history of a Kolsky bar experiment with a peak stress of 500 MPa. The nominal stress-rate is shown using the dashed-line and is computed by taking the slope of the stress-time curve between 10 % and 90 % of the peak stress. The stress-rate for this experiment is 30 MPa/μs. The strain rate may be approximated by dividing

the stress rate by the Young's modulus (E: Pa), resulting in a strain rate of approximately 430 s^{-1}. Also plotted with the stress-time curve are measurements of the axial (horizontal in the image- ε_{xx}) and lateral strains (vertical in the image- ε_{yy}). These are obtained using digital image correlation applied to the high-speed video images on the right. Also note that the times t_1 to t_6 are matched with the stress-time history and are plotted as blue dots on the left.

The dark regions on the surface of the sample in the video images are olivine grains (highlighted in Fig.2 image at time t_1). We first observe fracture located at the bottom right surface of the sample just prior to peak load (time t_2). The fracture appears to intersect one of the dark olivine grains on the surface. Correspondingly at t_2, the strains computed using digital image correlation are ε_{xx}=-0.9 % and ε_{yy}= 0.4 %. After peak stress (t_3), additional fractures on the surface are visible and, again, these intersect some of the olivine grains. As a result of the fractures, the stress in the sample collapses and the strains increase to ε_{xx}=-1.1 % and ε_{yy}= 0.9 % as a result of dilation. The coalescence of the fractures between the olivine grains is more clearly observed at t_4, where some additional fractures have also grown. The speed at which these cracks propagate is measured as 650 ±100 m/s. Note that not all of the cracks grow horizontally across the sample (i.e., in the direction of maximum compression). Pore collapse, material heterogeneity, local buckling and angular olivine defect shapes (see Fig. 1b) may contribute to the non-horizontal cracking. The strains in the sample at t_4 now increase at a faster rate, and are ε_{xx}=-1.3 % and ε_{yy}= 2.1 %. Cracks continue to grow and coalesce at t_5 and t_6, and the stress in the sample continues to collapse. By the time the stress has completely collapsed in the sample (i.e., around 40 μs), the strains are approximately ε_{xx}=-3.7% and ε_{yy}= 12%.

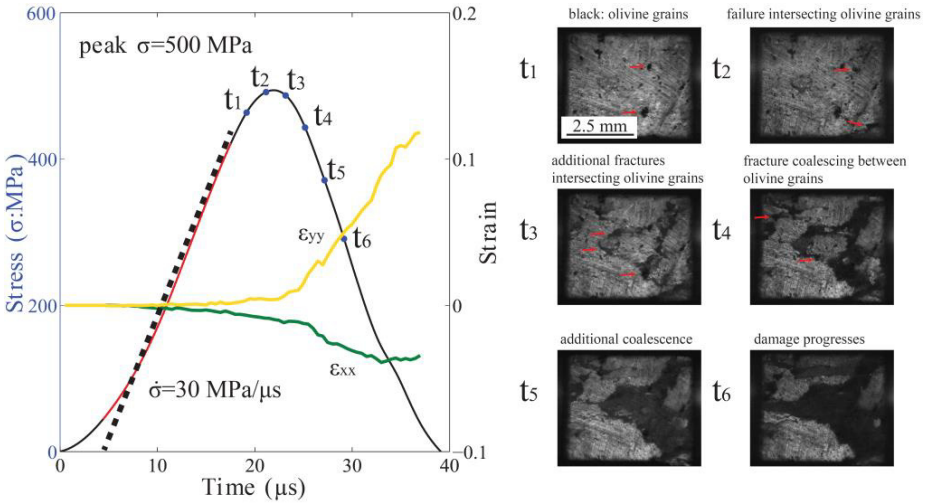

Fig. 2. Stress-time history of dynamic uniaxial compression of basalt (black curve) with time-resolved high-speed video images showing meso-scale failure mechanisms. The dashed line with the red underneath in the stress-time plot is the linear fit of 10 and 90 % of the peak stress and this corresponds to the stress-rate of 30 MPa/μs. The green curve is the associated axial strain (ε_{xx}), while the yellow curve is the lateral strain (ε_{yy}).

3.2. Quantification of Olivine Grains

Olivine grains have been identified as a potential defect contributing to the fracture and failure of the basalt. We provide some additional evidence in the image shown as an inset in Fig. 3a. To obtain this image, fragments collected from the intact experiment were mounted in resin and systematically polished to investigate internal features. In the inset image, olivine grains are observed to intersect the fracture surface at multiple locations inside of the fragment, and no internal fractures are observed. We believe this is evidence that olivine grains are contributing sites for fracture initiation, perhaps as a result of the hardness and stiffness mismatches between the olivine phase and the pyroxene and feldspar phases, although studies are still on-going to verify this.

Once olivine grains are identified as key defects, the next step is to quantify them so that we can relate their characteristics to fragmentation mechanisms. This also allows us to document their microstructure, which is not something commonly done. Image processing techniques are applied to a collection of microstructure images (an example shown in Fig. 1b) and the half-flaw size (s: μm), areal flaw density (#/m^2), and spacing between the defects (μm) are computed. Shown in Fig 3a is the cumulative distribution of olivine grain sizes, given by the variable s. Note here that the major axis dimension of the olivine grain is denoted as 2s, and we are plotting half of this because inputs for numerical models are commonly taken as the half-flaw size. We use the following cumulative distribution function $G(s)$ to fit the data:

$$G(s) = \left[\frac{1}{1+\left(\frac{s-s_{min}}{s'}\right)^{n}}\right] \tag{2}$$

where s_{min} is the minimum size considered, and s' and n are scaling parameters that are fit to the data. Other functions were attempted (exponential, lognormal), and the function in equation (2) was chosen because it fits the data adequately, with values of s_{min}=5 μm, s'=10 μm and n=-2.3.

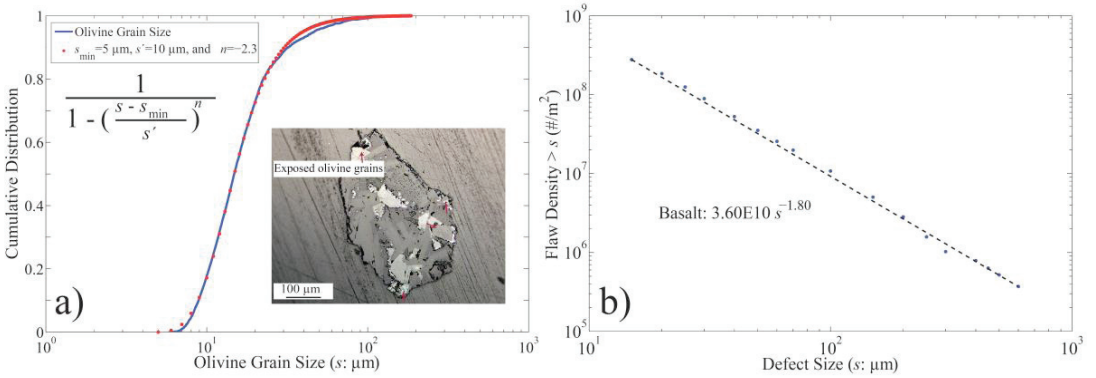

Fig. 3. (a) Cumulative distribution of olivine grain sizes with distribution fit, and inset of optical microscope image of internal features of a basalt fragment highlighting olivine grains intersecting the fracture surface. The blue line is the experimental measurements, while the red dots are the fitted distribution. (b) Areal flaw density (#/m^2) of olivine grains for sizes larger than s (blue dots) with power-law curve-fit shown using the hashed-line.

Next, we plot the areal defect density (#/m^2) of flaws larger than those on the corresponding x-axis (Fig. 3b). This is denoted as η>s. A power-law fit is used to fit the data:

$$\eta > s(s) = Cs^{D}$$

where C is the scaling parameter and D is the fractural dimension. The data is fitted well with C=3.6E10 and D=-1.80.

3.3. Dynamic Fragmentation of Intact Basalt

We examine dynamic fragmentation results in Fig. 4a, where we plot the cumulative distribution of fragments (red dashed-line) for fragments larger than approximately 10 μm. The first thing we observe is an inflection point in the distribution at around 100 μm, suggesting there are two different fragmentation mechanisms. To investigate this further, we also plot the cumulative distribution of spacing between adjacent olivine grains. It appears that the offset of the spacing distribution approximately corresponds to the inflection observed in the fragment size distribution. This suggests that there is a direct relationship between the olivine grain spacing and the resulting fragment sizes for sizes less than 100 μm. This appears reasonable since fractures initiated from olivine grains will likely coalesce with fractures initiated from adjacent olivine grains. Their coalescence will form a fragment size that is approximately equal to the spacing between grains.

Next, we examine the two different fragmentation mechanisms by considering a scatterplot of the mean greyscale color intensity against fragment size (Fig. 4b). The two different fragmentation mechanisms become more clearly defined and we describe the two regimes as follows: **I.** fragments < 100 μm in size that are related to the defect spacing between olivine grains. These fragments are optically bright (as they have high greyscale intensities), and, thus, these fragments are believed to be primarily comprised of pyroxene. Pyroxene is the weakest mineral phase in this material. The composition of these smaller fragments has also been confirmed with scanning electron microscopy and Energy Dispersive Spectroscopy. **II.** Fragments > 100 μm that are believed to form from the coalescence of the macro-fractures observed in the high-speed video image (Fig. 2). The fragments in this regime are controlled by the structural failure of the sample, which are, in turn, dependent on the stress-state and strain rate.

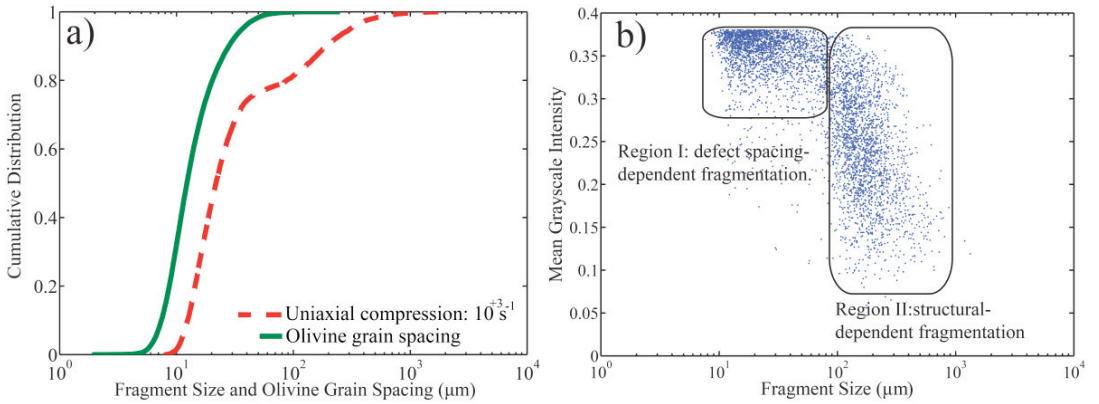

Fig. 4. (a) Cumulative distribution of dynamic uniaxial compressive fragmentation sizes and spacing between adjacent olivine grains. (b) Scatter plot of mean greyscale color intensity and size with two regimes labeled.

3.4. Dynamic Strength of Granular Basalt

In this final subsection we investigate the effect of the initial fragment size distribution on the strength of the fragmented material. We consider three distributions of fragments, each of which are shown in Fig 5a. Fragments were sieved for: 1. 10<L< 100 μm (average: 26 ± 11 μm), 2. 200 μm < L< 800 μm (average: 408 ± 145 μm), and 3. 300 μm < L< 1,800 μm (average: 988 ± 422 μm). The porosity, Φ, of the samples before loading is estimated as:

$$\Phi = 1 - \frac{\rho_{frag}}{\rho_{intact}} = 1 - \frac{m_{frag}/\nabla_{gage}}{\rho_{intact}} \tag{4}$$

where ρ is the density (kg/m^3), m_{frag} is the mass of fragments (kg) being tests, and ∇_{gage} is the volume (m^3) of the gage section of the heat shrink tubing in which materials are being tested. The porosities of the three granular samples are estimated as 30 %, 32 %, and 35 %, respectively. The corresponding stress-time response of the three different granular samples are shown in Fig. 5b. The peak strength of the material increases for decreasing fragment size from 4 MPa for larger fragment sizes, to 25 MPa for the intermediate size conditions, to 175 MPa for the smallest set of fragments tested. We note here that these are preliminary results and additional tests are needed.

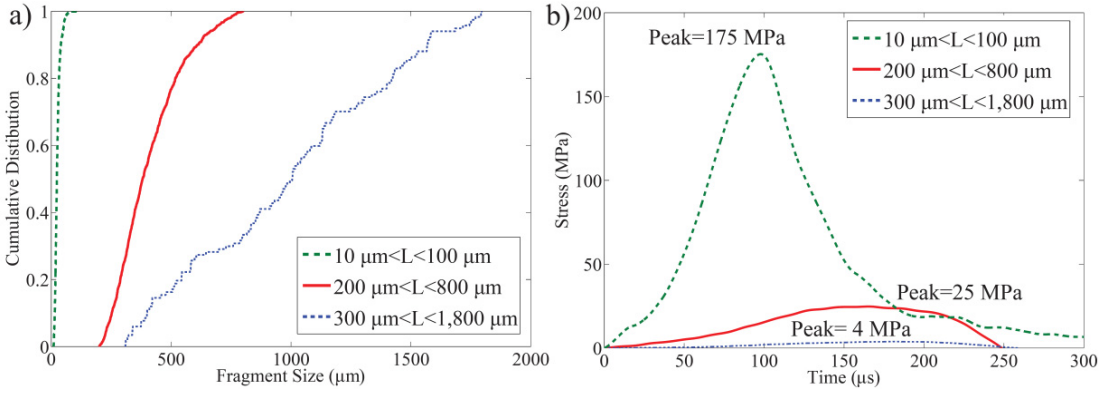

Fig. 5 (a) Cumulative distribution of fragment sizes used as initial conditions for compressive granular tests. (b) Stress-time history of compressive granular tests for different initial conditions of fragment sizes.

4. Summary and Implications

The role of the microstructure on the dynamic compressive failure and fragmentation of basalt has been examined. Real-time failure processes were tracked with high-speed photography, and these were linked with stress-time and strain measurements in order to understand the high-rate deformation of the basalt. Strains at peak stress are ε_{xx}=-0.9 % and ε_{yy}= 0.4 %. By the time the stress has completely collapsed in the sample, the strains are approximately ε_{xx}=-3.7 % and ε_{yy}= 12 %. Crack speeds were also measured (650 ±100 m/s), and these are important because, when coupled with a length scale (e.g. defect spacing), they provide guidance into inherent time scales associated with brittle failure.

High-speed photography was also used to identify olivine grains as sites for fracture initiation in basalt, and this is believed to be a result of the hardness and stiffness mismatches between the olivine and the adjacent grains. In order to better quantify the defect population, image processing techniques were used to determine the size and areal density (#/m^2) of the olivine grains, as well as the spacing between adjacent grains. Distributions were fit to the size and areal defect density results, while the spacing between grains was compared with fragment sizes. The quantification of defects provides insight into the olivine grain defect population in the basalt, and this is important when strength measurements and failure processes for different basalts are contrasted, and in the computational modelling of large-scale impact events into basaltic material.

The consequences of the microstructure on dynamic compressive fragmentation were considered in detail, and two fragmentation mechanisms were noted: **I.** A mechanism that generates smaller fragments comprised primarily of the weakest mineral phase (i.e. pyroxene) that is related to spacing between a critically activated type of defect (i.e., olivine grains); **II.** A mechanism that generates larger fragments associated with the structural failure of the sample. The fragments in this regime are polyphase and polygrain in nature. These results highlight the importance of the material microstructure on the dynamic compressive failure of planetary materials. In particular, the weakest mineral phase (in terms of fracture toughness) is preferentially fragmented to form the smaller fragments, and the sizes of these fragments are controlled by the spacing between some critically activated defects. In contrast, the sizes in Regime **II** are governed by the structural failure mechanisms that are activated during loading, which are dependent on stress-state and geometry. The initial fragmentation of the bulk material (in terms of size and composition) may have an effect upon the subsequent strength of the fragmented material.

The strength of the fragmented material was examined for three different size ranges: 1. 10 <L< 100 (average: 26 ± 11 μm), 2. 200 μm < L< 800 μm (average: 408 ± 145 μm), and 3. 300 μm < L< 1,800 μm (average: 988 ± 422 μm). Again, the smaller fragment class are primarily comprised of pyroxene grains, while the intermediate and larger classes are comprised of polyphase and polygrain fragments made up of a combination of olivine, pyroxene and feldspar. The strength of the material was observed to increase for decreasing fragment size from 4 to 25 to 175 MPa. These strengths are < 1 %, 5 %, and 35 % of the strength of the intact material, indicating: 1. mm-sized sized fragments have little to no strength, 2. the smallest fragments maintain notable strength, and 3. any impact into fragmented material (e.g., regolith on the lunar surface) would experience a range of strengths and failure mechanisms, and these should be considered in any such simulation. We note here that on-going work is needed across a wider range of conditions to confirm these interpretations.

Interestingly, there is a greater increase in strength between the intermediate and smaller fragment subsets than between the larger fragments and the intermediate fragments. It is understood that the contribution of frictional dissipation increases for smaller fragments, and the relative contribution of compaction and breaking decrease. However, we note that inherent defect population will also change as the fragment size is reduced, and this reduction in defect size will affect the strength of the fragmented material. As an example, the smaller pyroxene (<100 μm in size) in our basalt material will contain different and likely smaller defects than those fragments larger than 100 μm (which contain olivine grains). Altogether, the composition and defect statistics associated with the fragmented material should be considered when developing constitutive relation describing the strength of fragmented material.

5. Concluding Remarks

The role of the microstructure on the dynamic compressive failure and fragmentation of basalt has been examined. We have demonstrated the importance of the microstructure (composition and defect population) on the inherent length and time scales arising from the failure and fragmentation of planetary materials. The initial fragmentation, in terms of resulting composition and size, has been shown to have significant effects on the subsequent strength of the fragmented, and this should be considered in any development of constitutive relations for fragmented materials.

Acknowledgements

This material is based upon work supported by the National Aeronautics and Space Administration under grant NNX09AE39G issued through the Planetary Geology and Geophysics. This work was also supported by the Solar System Exploration Research Virtual Institute (SSERVI) NASA Cooperative Agreement NNA14AB02A for the Volatiles, Regolith and Thermal Investigations Consortium for Exploration and Science (VORTICES). This is SSERVI publication number SSERVI-2014-273. Joey Tilson and Kevin Peters are thanked for their efforts in analyzing fragment distributions and in helping conduct the experiments.

References

[1] Hörz, F., Cintala, M., 1997. Impact experiments related to the evolution of planetary regoliths, Meteoritics and Planetary Science 32 (2), p. 179–209.
[2] Michel, P., Benz, W., Richardson, D. C., 2003. Disruption of fragmented parent bodies as the origin of asteroid families, Nature 421 (6923), p. 608–611.
[3] Hogan, J.D., Plescia, J., Ramesh, K.T., 2014. Failure and fragmentation of meteorites and basalt: understanding lunar regolith generation, Lunar and Planetary Science Conference Abstracts, Vol. 45, Abstract 2426.
[4] Delbo, M., Libourel, G., Wilkerson, J., Murdoch, N., Michel, P., Ramesh. K.T., Ganino, C., Verati, C., Marchi S., 2014. Thermal fatigue as the origin of regolith on small asteroids, Nature 508, (7495), p. 233-236.
[5] Haggerty, S. E., 1978. The redox state of planetary basalts. Geophysical Research Letters 5 (6), p. 443–446.
[6] Ernst, C.M., Barnouin, O., Ramesh, K.T., Swaminathan, P.K., Kimberley, J., 2009, Lunar and Planetary Science Conference Abstracts, Vol. 40, Abstract 2523.
[7] Eberl, C., Thompson, R., Gianola, D., Sharpe Jr, W., Hemker, K., 2006. Digital image correlation and tracking, MatLabCentral, Mathworks file exchange server, FileID 565 12413.
[8] Kimberley, J., Ramesh, K. T., 2011. The dynamic strength of an ordinary chondrite, Meteoritics and Planetary Science, 46 (11) p. 1653–1669.
[9] Song, B., Weinong C., and Vincent L., 2009. Impact compressive response of dry sand, Mechanics of Materials 41 (6), p. 777-785.
[10] Stickle, A., Kimberley, J., Ramesh, K.T., 2013. Dynamic strength experiments on basalt with applications to cratering on Mercury, Lunar and Planetary Science Conference Abstracts, Vol. 44, Abstract 3021.
[11] Hogan, J.D., Rogers, R. J., Spray, J. G., Boonsue, S., 2012. Dynamic fragmentation of granite for impact energies of 6 to 28 J. Engineering Fracture Mechanics 79 (1), p.103-125.